

Quadrupolar charge dynamics in the nonmagnetic FeSe_{1-x}S_x superconductors

Weilu Zhang^{a,b,1} , Shangfei Wu^a , Shigeru Kasahara^{c,2} , Takasada Shibauchi^d , Yuji Matsuda^c , and Girsh Blumberg^{a,e,1} 

^aDepartment of Physics & Astronomy, Rutgers University, Piscataway, NJ 08854; ^bDepartment of Engineering and Applied Sciences, Sophia University, Tokyo 102-8554, Japan; ^cDepartment of Physics, Kyoto University, Kyoto 606-8502, Japan; ^dDepartment of Advanced Materials Science, University of Tokyo, Kashiwa 277-8561, Japan; and ^eNational Institute of Chemical Physics and Biophysics, 12618 Tallinn, Estonia

Edited by J. C. Séamus Davis, University of Oxford, Oxford, United Kingdom, and approved April 6, 2021 (received for review October 7, 2020)

We use polarization-resolved electronic Raman spectroscopy to study quadrupolar charge dynamics in a nonmagnetic FeSe_{1-x}S_x superconductor. We observe two types of long-wavelength XY symmetry excitations: 1) a low-energy quasi-elastic scattering peak (QEP) and 2) a broad electronic continuum with a maximum at 55 meV. Below the tetragonal-to-orthorhombic structural transition at $T_S(x)$, a pseudogap suppression with temperature dependence reminiscent of the nematic order parameter develops in the XY symmetry spectra of the electronic excitation continuum. The QEP exhibits critical enhancement upon cooling toward $T_S(x)$. The intensity of the QEP grows with increasing sulfur concentration x and maximizes near critical concentration $x_{cr} \approx 0.16$, while the pseudogap size decreases with the suppression of $T_S(x)$. We interpret the development of the pseudogap in the quadrupole scattering channel as a manifestation of transition from the non-Fermi liquid regime, dominated by strong Pomeranchuk-like fluctuations giving rise to intense electronic continuum of excitations in the fourfold symmetric high-temperature phase, to the Fermi liquid regime in the broken-symmetry nematic phase where the quadrupole fluctuations are suppressed.

nematic order | Pomeranchuk instability | non-Fermi liquid | superconductivity | Raman spectroscopy

The iron-based superconductors (FeSCs) exhibit a complex phase diagram with multiple competing orders. For most of the FeSCs, an electronic nematic phase transition takes place at T_S , which is followed by a magnetic phase transition at T_N (1–4). Superconductivity emerges in close proximity to the electronic nematic and the antiferromagnetic orders. The highest superconducting (SC) transition temperature T_c often occurs when nematic and magnetic orders are fully suppressed but the orbital/charge or spin fluctuations remain strong (5–10). The relationship between these fluctuations and superconductivity has been the focus of intense research (4, 6, 11–31).

The family of FeSe superconductors is the simplest system to elucidate the origin of orbital and charge fluctuations because for these materials nematicity appears in the absence of magnetic order (13, 32, 33). At the ambient pressure, a structural phase transition that breaks the fourfold rotational symmetry (C_4) takes place at $T_S = 90$ K. Strong electronic quadrupole fluctuations involving the charge transfer between the degenerate Fe $3d_{xz}$ and $3d_{yz}$ orbitals, which contribute to most of the electronic density of states near E_F , have been observed above T_S (18, 34–36). The degeneracy of the d_{xz} and d_{yz} orbitals is lifted in the symmetry-broken phase (37–39), where although the lattice is only weakly distorted, a prominent anisotropy of the electronic properties was detected (22, 40, 41). For single crystals, superconductivity emerges in the nematic phase at $T_c \approx 9$ K (32), while for FeSe monolayer films deposited on SrTiO₃ substrate the T_c can be enhanced by almost an order of magnitude (42–45). An unusual orbital-selective SC pairing has been reported by angle-resolved photo-emission spectroscopy (ARPES) and quasiparticle interference (QPI) studies in bulk

FeSe: The SC gap energy is large only at a specific region of the nematic Fermi surfaces with the Fe $3d_{yz}$ orbital characters (22, 40, 41, 45).

Partial isovalent sulfur substitution at the selenium site monotonically suppresses the structural phase transition temperature T_S until it vanishes at the critical concentration $x_{cr} \approx 0.16$, while the SC transition temperature T_c first mildly increases with substitution and reaches maximum value 11 K at $x = 0.08$ (22, 23, 34). Thus, the phase diagram of FeSe_{1-x}S_x alloys enables a spectroscopic study of the interplay between competing ordered phases.

In this work we employ polarization-resolved Raman spectroscopy to study charge quadrupole dynamics in the nonmagnetic superconductor alloy FeSe_{1-x}S_x (10, 34). We observe two main features in the XY symmetry scattering channel: 1) a low-energy quasi-elastic scattering peak (QEP) that, above $T_S(x)$, exhibits enhancement and softening upon cooling in a wide temperature and sulfur doping range and 2) a high-energy electronic continuum extending beyond 2,000 cm⁻¹ with a broad peak at 450 cm⁻¹ that arises due to beyond Fermi-liquid Pomeranchuk-like XY-quadrupole fluctuations in the high-temperature fourfold symmetric phase. The Fermi-liquid regime recovers in the low-temperature nematic phase where the

Significance

The family of iron selenide (FeSe) superconductors is of great interest because it harbors an unusual nonmagnetic nematic state, exhibits a peculiar orbital-selective Cooper pairing, and has a strong potential for high-temperature superconductivity. Here, for FeSe_{1-x}S_x nonmagnetic metal, we report discovery of a pseudogap in the spectra of electronic long-wavelength charge quadrupole excitation below the nematic phase transition with temperature dependence of the gap's magnitude reminiscent of a nematic order parameter. We argue that the intense continuum of excitations in the high-temperature phase with tetragonal symmetry arises due to non-Fermi liquid dynamics governed by Pomeranchuk fluctuations and that these fluctuations are suppressed in the symmetry-broken orthorhombic low-temperature phase, enabling the recovery of Fermi liquid properties.

Author contributions: W.Z. and G.B. designed research; W.Z., S.W., S.K., T.S., Y.M., and G.B. performed research; W.Z., S.W., and G.B. analyzed data; W.Z., S.W., and G.B. wrote the paper; and S.K., T.S., and Y.M. made the samples.

The authors declare no competing interest.

This article is a PNAS Direct Submission.

Published under the PNAS license.

¹To whom correspondence may be addressed. Email: girsh@physics.rutgers.edu or weiluzhang41@gmail.com.

²Present address: Research Institute for Interdisciplinary Science, Okayama University, Okayama 700-8530, Japan.

This article contains supporting information online at <https://www.pnas.org/lookup/suppl/doi:10.1073/pnas.2020585118/-/DCSupplemental>.

Published May 12, 2021.

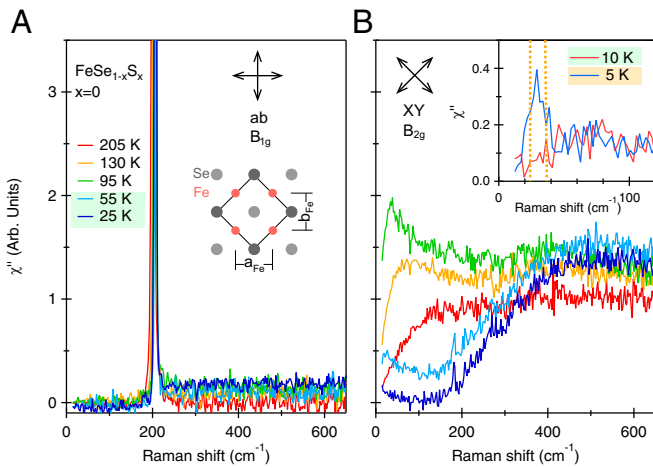


Fig. 1. Temperature evolution of the B_{1g} (ab) and B_{2g} (XY) symmetry Raman response $\chi''(\omega, T)$ for undoped FeSe. *A*, Inset shows the top view of the FeSe layer. Dark and light gray circles represent the Se above and below the Fe layer. The two-iron unit cell for the high-temperature phase is shown by solid lines. In the low-temperature phase, the nearest Fe-Fe bonding distance a_{Fe} becomes larger than b_{Fe} while a_{Fe} and b_{Fe} remain orthogonal. *B*, Inset shows $\chi''(\omega, T)$ in the XY symmetry channel of FeSe in the normal state (red, 10 K) and the SC state (blue, 5 K). The magnitude of the two SC gaps $2\Delta_{SC} = 3$ and 4.6 meV measured by tunneling spectroscopy are shown with the vertical dotted lines (*SI Appendix* and ref. 41).

low-frequency quadrupole fluctuations are suppressed, causing an apparent pseudogap in the electronic continuum for metals with small but prominent Fermi surface pockets.

Results

In Fig. 1 *A* and *B* we show temperature dependence of the Raman response for undoped FeSe in B_{1g} (ab) and B_{2g} (XY) symmetry channels (D_{4h} point group) defined for a two-iron unit cell. The data for the B_{1g} channel are composed of the Fe phonon mode at 195 cm^{-1} (12) above a weak temperature independent continuum background (Fig. 1*A*). In contrast, the electronic Raman continuum in the B_{2g} channel is strong (Figs. 1*B* and 2); it is composed of several spectral features:

- 1) A low-energy QEP. The intensity of the QEP is weak at high temperatures. Upon cooling, the QEP softens from about 100 down to a few tens of cm^{-1} , gains intensity, reaches its maximum intensity just above T_S , and then gradually loses its intensity below T_S , the blue component in Fig. 2*B*. In the SC phase, the QEP acquires coherence and undergoes a metamorphosis into an in-gap collective mode (Fig. 1 *B*, Inset) similar to several other FeSC superconductors (17, 51–54).
- 2) A broad electronic continuum extending beyond $2,000 \text{ cm}^{-1}$ with the intensity peaking at about 450 cm^{-1} and showing only weak dependence on temperature and doping (the yellow component in Fig. 2 *B1–B5* and Fig. 3 *A* and *B*).
- 3) Below T_S , a significant pseudogap-like suppression develops at frequencies below 400 cm^{-1} (Figs. 2 and 3*A*).
- 4) On approach to $T_S(x)$ an additional sharp low-frequency feature appears that is most pronounced for the alloys with high sulfur concentration, shown in violet in Fig. 2 *B1–B5*. The mode could be attributed to the lattice dynamics above $T_S(x)$ governed by back and forth fluctuation between two short-range nematic distortion domains (47, 48) which break the symmetry in the opposite sense in the presence of local defects due to sulfur substi-

tion, a feature typical for displacive structural phase transitions (46).

- 5) An additional intensity which develops below $T_S(x)$ at the lowest frequencies and is related to coupling between QEP response and acoustic lattice modes in the presence of a quasiperiodic array of the structural domain walls that appear in twinned crystals (55).
- 6) A weak feature at about 190 cm^{-1} that is related to interband transition between occupied β and unoccupied α bands (31).

In Fig. 2, we show doping dependence of XY Raman response for $\text{FeSe}_{1-x}\text{S}_x$ with five sulfur concentrations. For $x < 0.16$ alloys the tetragonal-to-orthorhombic structural phase transition temperature $T_S(x)$ (34) is marked in Fig. 2 *A1–A4*. For all concentrations $x < 0.16$, we observe an enhancement and critical softening of the QEP upon cooling toward T_S . Upon entering into the orthorhombic phase, intensity of the QEP diminishes and a pseudogap-like suppression develops at low frequencies. At the lowest temperature, a full gap suppression appears in the continuum for all samples with substitution concentrations $x < 0.15$. For $x = 0.15$, some residual scattering intensity remains in the gap. The energy of gap-like suppression onset (Fig. 2 *B1–B4*) appears to be close to the $d_{xz/yz}$ orbital splitting near the electron pocket in the nematic phase, as was reported by ARPES (Fig. 2 *B1–B4*) (49, 50). For the $x = 0.20$ sample which remains tetragonal in the whole temperature range, no gap-like suppression is observed in the Raman spectra (Figs. 2 *B5* and 3*B*).

The peak in the broad continuum at about 450 cm^{-1} appears at low temperatures for crystals with all sulfur compositions x . In Fig. 3 we show a comparison of XY -symmetry Raman response for pristine FeSe ($x = 0$, $T_S = 88 \text{ K}$) and heavily sulfur substituted ($x = 0.20$) crystals. The 450-cm^{-1} feature can be followed for both samples at all measured temperatures, in both tetragonal and orthorhombic phases. More importantly, for each given temperature the feature's line shape is quite similar for both samples: The only distinction between the data in tetragonal and orthorhombic phases is the pseudogap-like suppression which develops below T_S . Thus, this broad feature is not exclusive for the nematic phase (*SI Appendix, Doping Dependence of the 450 cm^{-1} Feature*).

Discussion

We model the XY -symmetry electronic Raman response containing the QEP and the 450-cm^{-1} features by two main Raman oscillators with frequency-dependent self-energy (Figs. 2 *B1–B5* and 3) (*SI Appendix, Data Fit*). In the tetragonal phase, the following form of self-energy provides the best data description:

$$\Sigma''(\omega, T) = m_0\omega + n_0T, \quad \text{if } T > T_S(x). \quad [1]$$

The Fermi-liquid-like frequency dependence recovers in the low-temperature nematic phase, the green region in the phase diagram in Fig. 4*D*, where the self-energy

$$\Sigma''(\omega, T) = \begin{cases} m_0\omega^2/\omega_c(T, x) + n_0T, & \text{if } \omega < \omega_c(T, x) \\ m_0\omega + n_0T, & \text{if } \omega > \omega_c(T, x) \end{cases} \quad [2]$$

represents the data best (Figs. 2 and 3). Here $m_0 = 1.2$, $n_0 = 1.5 \text{ cm}^{-1}/\text{K}$, and $\omega_c(T, x)$ labels the cross-over frequency which evolves with temperature and sulfur doping, as shown in Fig. 4*C*, similar to the onset energy of the pseudogap suppression. Consistent with this result, a low-temperature cross-over from quasi- T -linear to T^2 Fermi-liquid-like behavior was also reported for resistivity measurements $\rho(T, x)$ if $x < 0.16$ in the orthorhombic phase (23, 24).

We note here that the appearance of a strong low-frequency mode with the lattice involvement, especially for the $x = 0.2$ sam-

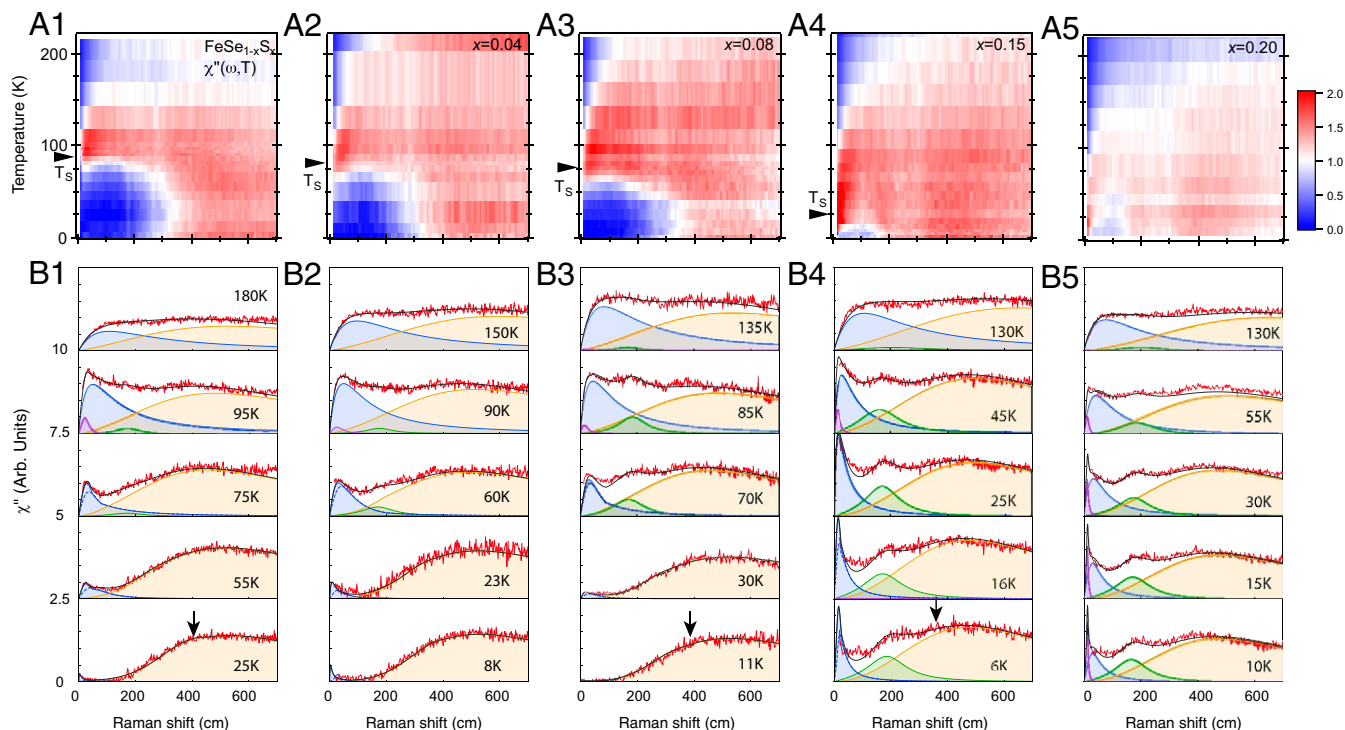


Fig. 2. (A1–A5) Temperature evolution of Raman susceptibility $\chi''_{XY}(\omega, T)$ in the XY symmetry channel for $\text{FeSe}_{1-x}\text{S}_x$ ($x = 0, 0.04, 0.08, 0.15,$ and 0.2). The arrows at the temperature axis denote $T_S(x)$. (B1–B5) $\chi''_{XY}(\omega, T)$ data (red) at representative temperatures and the fits (black) to the sum of the oscillators model. The QEP contribution is shaded in blue; contribution of the strongly overdamped high-energy electronic oscillator is shaded in yellow. A feature due to interband transition at about 190 cm^{-1} is shown in green. The additional low-frequency oscillator due to local lattice dynamics coupled to the fluctuating order parameter above $T_S(x)$ (46–48) is shown in purple. Below $T_S(x)$, the coupled acoustic lattice mode and the QEP (shaded in blue) add additional low-frequency spectral weight to the QEP (blue dashed lines). The arrows in B1, B3, and B4 indicate the energy of nematic d_{xz}/d_{yz} orbital splitting reported in ARPES studies (49, 50).

ple (purple shading in the phase diagram, Fig. 4D), is expected to quench the long-wavelength nematic fluctuations at low frequency (56–59), giving rise to recovery of T^2 -like resistivity with a significant residual value ρ_0 , again consistent with the data in refs. 23 and 24.

Next, in Fig. 4A1–A5 we plot temperature dependence of the static electronic Raman susceptibility for the QEP and the continuum contributions $\chi_{QEP}(0, T)$ and $\chi_C(0, T)$ that we derive from the spectra by Kramers–Kronig transformation:

$$\chi(0, T) = \frac{2}{\pi} P \int_0^{\omega_{uv}} \frac{\chi''(\omega, T)}{\omega} d\omega, \quad [3]$$

where we choose high-energy cutoff ω_{uv} at $2,000 \text{ cm}^{-1}$ (SI Appendix, Static Susceptibility). In contrast to mild temperature evolution of the continuum contribution $\chi_C(0, T)$, a critical enhancement upon cooling toward $T_S(x)$ is clearly observed for the QEP component of the static susceptibility. We fit the latter by an inverse power law

$$1/\chi_{QEP}(0, T > T_S) = f(T) \propto \left[\frac{T - T_{QEP}(x)}{T_0} \right]^{-2} + C, \quad [4]$$

(Fig. 4B1–B5), where critical temperature $T_{QEP}(x)$ is shown in Fig. 4D and T_0 is an effective temperature about 220 K. Note that the non-Curie–Weiss form of susceptibility arises due to self-energy effects in the tetragonal phase.

The temperature dependence of the low-frequency QEP fluctuations has been meticulously studied for generic FeSC (6, 17, 18, 26, 60, 61). The behavior arises from degeneracy of the partially filled iron $3d_{xz}$ and $3d_{yz}$ orbitals in the tetragonal phase (62–64). The QEP is related to overdamped dynamical charge

oscillations at sub-terahertz frequencies, which give rise to a fluctuating charge quadrupole moment with an amplitude proportional to oscillating d_{xz}/d_{yz} orbital charge imbalance $Q \propto n_{xz} - n_{yz}$, where $n_{xz/yz}$ is the orbital occupancy (16, 17, 60, 65–70). Such excitations result in Pomeranchuk-like nematic

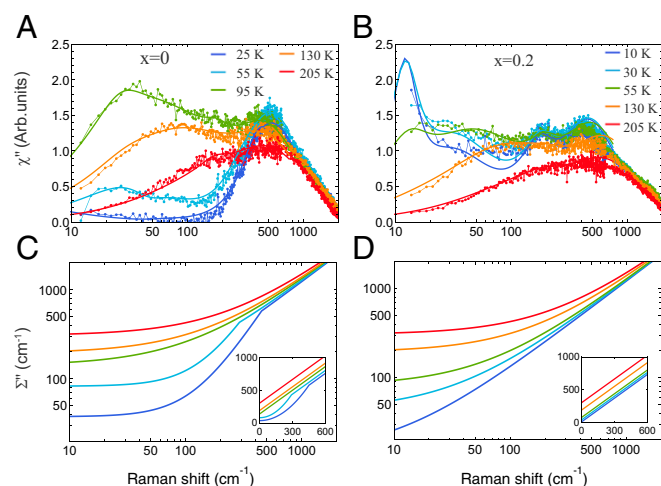


Fig. 3. (A and B) Temperature evolution of the $\chi''_{XY}(\omega, T)$ Raman response data and the fits to a model of oscillators (SI Appendix, Data Fit) for stoichiometric FeSe in A and for $\text{FeSe}_{0.8}\text{S}_{0.2}$ in B. (C and D) The imaginary part of self-energy $\Sigma''(\omega, T)$ used for the data fits in A and B correspondingly. Insets show a zoom-in of the low-frequency region for $\Sigma''(\omega, T)$ in linear scale.

dynamic deformation of the Fermi surface pockets with nodal lines in the X/Y directions (see illustration of a snapshot in Fig. 5C). These Pomeranchuk-like quadrupole fluctuations are strongly overdamped in the normal state leading to the QEP feature, while in the SC state, when low-energy relaxation is removed, the QEP feature transforms into a sharp in-gap collective mode (17, 53). For pnictides, the temperature dependence of the bare static electronic susceptibility $\chi_{QEP}(0, T)$ often shows critical behavior on its own (17, 71), leading to a d -wave Pomeranchuk instability at enhanced temperature T_S as a result of coupling to the lattice (14, 16). In the low-temperature orthorhombic phase, the fourfold rotational symmetry on the Fe site is broken and hence the degeneracy of Fe $3d_{xz}$ and $3d_{yz}$ is lifted, which causes rapid suppression of the low-energy fluctuations.

To explain the two components in $\text{FeSe}_{1-x}\text{S}_x$ spectra we construct a nominal model containing one hole FS pocket at the Γ point and one electron pocket at the M point consisting only of d_{xz} and d_{yz} orbital characters (Fig. 5). The two FS pockets give rise to two types of Pomeranchuk oscillations: in phase (Fig. 5B) and antiphase (Fig. 5C). We define two order parameters $\phi_1 = \phi_\Gamma + \phi_M$ and $\phi_2 = \phi_\Gamma - \phi_M$, which depict these fluctuation phases, respectively.

For the tetragonal phase above $T_S(x)$, the fluctuations of the two order parameters around free-energy minima (ϕ_1, ϕ_2) = (0,0) give rise to the XY -symmetry Raman response (Fig.

5D). The critical oscillations are in the direction with lowest free energy, they give rise to the QEP (feature 1), while the oscillation in the direction with the higher energy that is only weakly dependent on temperature and doping x results in the broad electronic Raman continuum peaked at about 450 cm^{-1} (feature 2).

In the nematic phase below T_S the system condenses into a state with minimal free energy determined by the relation between intrapocket nematic interaction and inter-pocket repulsion: If the former interaction prevails, the ϕ_1 in-phase arrangement wins; alternatively, if the inter-pocket repulsion is stronger than intrapocket nematic interaction, the ϕ_2 antiphase arrangement is the ground state (72). The recent ARPES study indicates that in the nematic phase the d_{xz} orbital dominates the FS pocket at the Γ point while the d_{yz} orbital dominates the pocket at the M point (50). Thus, the ϕ_2 antiphase FS distortion arrangement due to the inter-pocket repulsion is the prevailing order parameter (72) (Fig. 5C). We also note that such configuration is antagonistic to a spin-density-wave order.

Hence, the ϕ_2 antiphase FS distortion fluctuations are responsible for both the critical quasi-elastic scattering in the tetragonal phase (72) and the in-gap collective mode in the SC phase (17). Then, the ϕ_1 -like in-phase fluctuations of the FS distortion give rise to the broad high-energy Raman continuum. When the d_{xz}/d_{yz} orbitals split in the ordered state below T_S

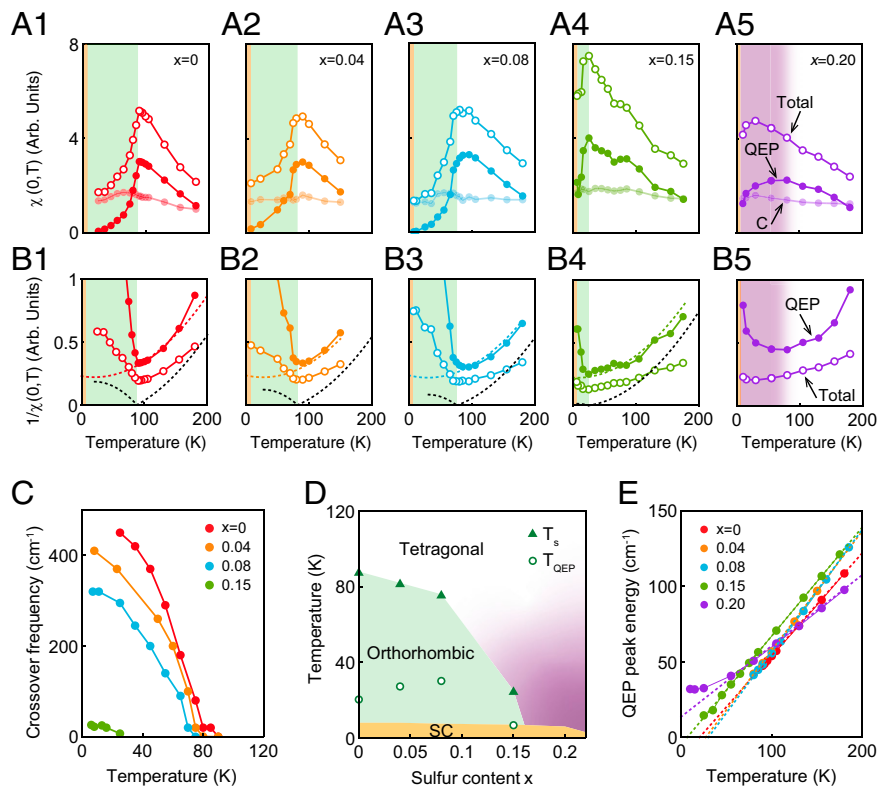


Fig. 4. (A1–A5) Two main contributions to the XY -symmetry static Raman susceptibility: $\chi_{QEP}(0, T)$ (solid circles) and $\chi_C(0, T)$ (shaded circles) for $x = 0, 0.04, 0.08, 0.15,$ and 0.2 . The open circles denote the total Raman static susceptibility (including all spectral features) obtained from the Raman data (Fig. 2). The green and yellow shades indicate temperature regions below $T_S(x)$ and $T_C(x)$ as shown in the phase diagram (D) (34). The purple shading in A5 and B5 denotes a region of phase diagram where the low-frequency fluctuations are significant (Fig. 2 and SI Appendix, Data Fit, section E). (B1–B5) Temperature dependence of the inverse static susceptibilities shown in A1–A5. The dashed black lines denote inverse total static susceptibilities including the lattice contribution, Eq. 6. (C) Temperature evolution of the cross-over to Fermi-liquid boundary $\omega_c(\omega, T)$. Color coding for the respective sulfur concentration x is same as in A1–A5. (D) The temperature–sulfur concentration phase diagram. $T_S(x)$ is the nematic phase transition temperature (34); $T_{QEP}(x)$ is the temperature where the QEP mode’s peak frequency would soften to zero, as determined by linear approximation from the high-temperature phase (E). (E) Temperature dependence of the QEP peak frequency. Dashed asymptotic lines define $T_{QEP}(x)$.

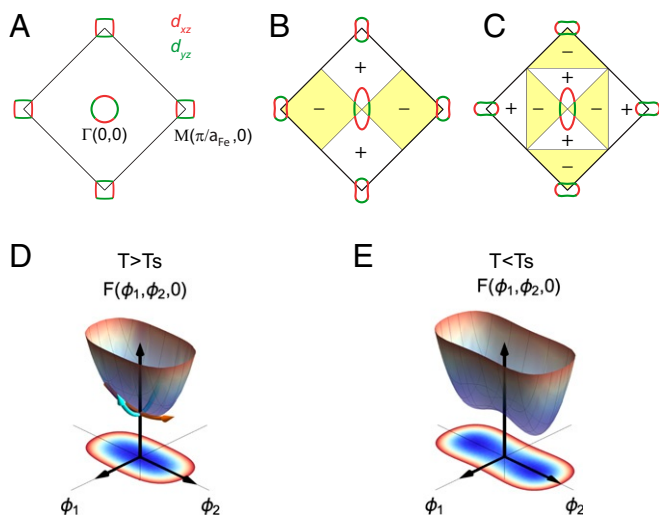


Fig. 5. (A) A minimal d_{xz} - d_{yz} two-orbital model consisting of a hole pocket at the Γ point and an electron pocket at the M point for the high-temperature tetragonal phase. (B and C) Illustrations of B_{2g} -symmetry in-phase and antiphase Fermi surface distortions. (D and E) Ginzburg-Landau free energy for the tetragonal phase and the nematic phase. The orange and cyan arrows in D represent the oscillations of the order parameters in the high-temperature phase that correspond to the QEP (feature 1) and the broad electronic continuum peaked at 450 cm^{-1} (feature 2) in the Raman spectra, respectively.

(37–39, 50, 73), stiffness of the dominant ϕ_2 order parameter suppresses the ϕ_1 -like quadrupole fluctuations at the frequencies below the orbital splitting energy, which naturally explains the recovery of the Fermi-liquid regime seen as the appearance of a pseudogap in the XY -symmetry Raman response (Figs. 2 and 3A).

In Fig. 5 D and E we show the free energy as a function of ϕ_1 and ϕ_2 for above and below T_S phases. Above T_S , the fluctuations of both order parameters ϕ_2 and ϕ_1 contribute to the Raman response consisting of the QEP at low energy and the high-energy continuum at around 450 cm^{-1} , respectively. Below T_S , the ϕ_2 becomes the dominant order, while the ϕ_1 -like fluctuations are suppressed at low energies.

Finally, we consider coupling of the critical ϕ_2 order parameter to the orthorhombic lattice strain ϵ by constructing a model free energy of the system (14):

$$F(\phi_2, \epsilon) = \frac{1}{2}f(T)\phi_2^2 + \frac{1}{4}\beta_2\phi_2^4 + \frac{C_{66,0}}{2}\epsilon^2 - \lambda\phi_2\epsilon, \quad [5]$$

where $f(T)$ is inverse bare electronic nematic susceptibility, λ is bilinear electron-lattice coupling between ϕ_2 and the orthorhombic lattice distortion ϵ with B_{2g} symmetry, and $C_{66,0}$ is lattice bare shear modulus. Here we neglect the contributions due to subdominant electronic order ϕ_1 .

In the following, we deduce the nematic susceptibility. To consider the coupling of the electronic order parameter ϕ_2 to the XY -symmetry Raman field A exerted by the XY polarized incident and scattered light, we add to free energy an interaction term $-\gamma\phi_2 A$, where γ is the interaction constant. Then, the

nematic susceptibility can be expressed as response of electronic order parameter ϕ_2 to perturbation A :

$$\chi_{nem}(T) = \frac{\partial\phi_2}{\partial A} = \begin{cases} \frac{\gamma}{[f(T)-f(T_S)]}, & \text{if } T > T_S \\ \frac{\gamma}{2[f(T_S)-f(T)]}, & \text{if } T_{QEP} < T < T_S \end{cases}, \quad [6]$$

where T_S is defined by the equation $f(T_S) = \lambda^2/C_{66,0}$. One can see from Fig. 4 B1–B4 that $f(T_S)$ and therefore the electron-lattice coupling λ only mildly depend on x . Thus, the collapse of $T_S(x)$ at the approach to x_{cr} is primarily caused by suppression of $T_{QEP}(x)$. We also note that superconducting $T_c(x)$ is not enhanced in the vicinity of x_{cr} ; instead, both $T_{QEP}(x)$ and $T_c(x)$ have a weak enhancement in the middle of the nematic phase (Fig. 4D).

In summary, we have demonstrated that polarization-resolved Raman spectroscopy provides detailed information on non-Fermi-liquid quadrupolar charge dynamics. In application to nonmagnetic $\text{FeSe}_{1-x}\text{S}_x$ superconductors, we argue that the intense XY -symmetry Raman continuum of excitations in the high-temperature tetragonal phase arises due to non-Fermi-liquid dynamics governed by Pomeranchuk fluctuations and that these fluctuations are suppressed in the symmetry-broken orthorhombic phase enabling the recovery of Fermi-liquid properties, in agreement with the transport studies (23). We further show that while the tetragonal-to-orthorhombic phase transition is driven by the Pomeranchuk fluctuation soft mode, coupling to the lattice significantly enhances the nematic transition temperature.

Materials and Methods

$\text{FeSe}_{1-x}\text{S}_x$ ($x = 0, 0.04, 0.08, 0.15$, and 0.2) single crystals were grown by the chemical vapor transport technique as described in ref. 34. Substitution of sulfur for selenium acts as negative pressure, which suppresses T_S while the system remains nonmagnetic, and superconductivity remains robust (10, 22, 34). Strain-free crystals were cleaved in a nitrogen atmosphere and positioned in a continuous-flow optical cryostat.

Polarization-resolved Raman spectra were acquired in a quasi-backscattering geometry from the ab surface. We used 2.6-eV excitation from a Kr^+ laser. The laser power was kept below 10 mW for most measurements and less than 2 mW for the measurements in the SC state. The laser heating $\approx 1\text{ K/mW}$ was estimated by the appearance of the stripe pattern on the crystal surface at T_S (61). The Raman scattering signal was analyzed by a custom triple-grating spectrometer and the data were corrected for the spectral response of the spectrometer.

Raman scattering spectra were acquired in three polarization configurations ($\mu\nu = XY, ab$, and aa) to separate excitations in distinct symmetry channels: $B_{1g} = ab$, $B_{2g} = XY$, and $A_{1g} = aa(bb) - XY$ (SI Appendix, Background Subtraction and SI Appendix, Doping Dependence of Phonon Spectra).

Data Availability. All study data are included in this article and/or SI Appendix.

ACKNOWLEDGMENTS. The spectroscopic work at Rutgers (W.Z., S.W., and G.B.) was supported by NSF Grant DMR-1709161. The sample growth and characterization work in Japan was supported by Grants-in-Aid for Scientific Research (no. JP18H01177, no. JP18H05227, and no. JP19H00649), Innovative Area “Quantum Liquid Crystals” (no. JP19H05824) from the Japan Society for the Promotion of Science, and by CREST (no. JPMJCR19T5) from Japan Science and Technology. The work at National Institute of Chemical Physics and Biophysics (NICPB) was supported by the European Research Council under Grant 885413.

1. E. Fradkin, S. A. Kivelson, M. J. Lawler, J. P. Eisenstein, A. P. Mackenzie, Nematic Fermi fluids in condensed matter physics. *Annu. Rev. Condens. Matter Phys.* **1**, 153–178 (2010).
2. G. R. Stewart, Superconductivity in iron compounds. *Rev. Mod. Phys.* **83**, 1589–1652 (2011).
3. J. Paglione, R. L. Greene, High-temperature superconductivity in iron-based materials. *Nat. Phys.* **6**, 645–658 (2010).

4. R. M. Fernandes, A. V. Chubukov, J. Schmalian, What drives nematic order in iron-based superconductors? *Nat. Phys.* **10**, 97–104 (2014).
5. J. H. Chu, H. H. Kuo, J. G. Analytis, I. R. Fisher, Divergent nematic susceptibility in an iron arsenide superconductor. *Science* **337**, 710–712 (2012).
6. Y. Gallais et al., Observation of incipient charge nematicity in $\text{Ba}(\text{Fe}_{1-x}\text{Co}_x)_2\text{As}_2$. *Phys. Rev. Lett.* **111**, 267001 (2013).

7. T. Shibauchi, A. Carrington, Y. Matsuda, A quantum critical point lying beneath the superconducting dome in iron pnictides. *Annu. Rev. Condens. Matter Phys.* **5**, 113–135 (2014).
8. A. E. Bohmer *et al.*, Nematic susceptibility of hole-doped and electron-doped BaFe_2As_2 iron-based superconductors from shear modulus measurements. *Phys. Rev. Lett.* **112**, 047001 (2014).
9. X. Lu *et al.*, Nematic spin correlations in the tetragonal state of uniaxial-strained $\text{BaFe}_2-x\text{Ni}_x\text{As}_2$. *Science* **345**, 657–660 (2014).
10. K. Matsuura *et al.*, Maximizing T_c by tuning nematicity and magnetism in $\text{FeSe}_{1-x}\text{S}_x$ superconductors. *Nat. Commun.* **8**, 1143 (2017).
11. S. Kasahara *et al.*, Electronic nematicity above the structural and superconducting transition in $\text{BaFe}_2(\text{As}_{1-x}\text{P}_x)_2$. *Nature* **486**, 382–385 (2012).
12. V. Gnezdilov *et al.*, Interplay between lattice and spin states degree of freedom in the FeSe superconductor: Dynamic spin state instabilities. *Phys. Rev. B* **87**, 144508 (2013).
13. S. H. Baek *et al.*, Orbital-driven nematicity in FeSe. *Nat. Mater.* **14**, 210–214 (2015).
14. A. E. Böhmner, C. Meingast, Electronic nematic susceptibility of iron-based superconductors. *Compt. Rendus Phys.* **17**, 90–112 (2016).
15. A. V. Chubukov, M. Khodas, R. M. Fernandes, Magnetism, superconductivity, and spontaneous orbital order in iron-based superconductors: Which comes first and why? *Phys. Rev. X* **6**, 041045 (2016).
16. Y. Gallais, I. Paul, Charge nematicity and electronic Raman scattering in iron-based superconductors. *Compt. Rendus Phys.* **17**, 113–139 (2016).
17. V. K. Thorsmølle *et al.*, Critical quadrupole fluctuations and collective modes in iron pnictide superconductors. *Phys. Rev. B* **93**, 054515 (2016).
18. P. Massat *et al.*, Charge-induced nematicity in FeSe. *Proc. Natl. Acad. Sci. U.S.A.* **113**, 9177–9181 (2016).
19. A. P. Dioguardi *et al.*, NMR evidence for inhomogeneous nematic fluctuations in $\text{BaFe}_2(\text{As}_{1-x}\text{P}_x)_2$. *Phys. Rev. Lett.* **116**, 107202 (2016).
20. Y. Schattner, S. Lederer, S. A. Kivelson, E. Berg, Ising nematic quantum critical point in a metal: A Monte Carlo study. *Phys. Rev. X* **6**, 031028 (2016).
21. L. Classen, R. Q. Xing, M. Khodas, A. V. Chubukov, Interplay between magnetism, superconductivity, and orbital order in 5-pocket model for iron-based superconductors: Parquet renormalization group study. *Phys. Rev. Lett.* **118**, 037001 (2017).
22. T. Hanaguri *et al.*, Two distinct superconducting pairing states divided by the nematic end point in $\text{FeSe}_{1-x}\text{S}_x$. *Sci. Adv.* **4**, eaar6419 (2018).
23. S. Licciardello *et al.*, Electrical resistivity across a nematic quantum critical point. *Nature* **567**, 213–217 (2019).
24. S. Licciardello *et al.*, Coexistence of orbital and quantum critical magnetoresistance in $\text{FeSe}_{1-x}\text{S}_x$. *Phys. Rev. Res.* **1**, 023011 (2019).
25. A. Baum *et al.*, Frustrated spin order and stripe fluctuations in FeSe. *Commun. Phys.* **2**, 14 (2019).
26. S. Chibani *et al.*, Lattice-shifted nematic quantum critical point in $\text{FeSe}_{1-x}\text{S}_x$. *NPJ Quantum Mater.* **6**, 37 (2021).
27. A. Kreisel, P. J. Hirschfeld, B. M. Andersen, On the remarkable superconductivity of FeSe and its close cousins. *Symmetry* **12**, 1402 (2020).
28. T. Shibauchi, T. Hanaguri, Y. Matsuda, Exotic superconducting states in FeSe-based materials. *J. Phys. Soc. Jpn.* **89**, 102002 (2020).
29. N. Lazarević, R. Hackl, Fluctuations and pairing in Fe-based superconductors: Light scattering experiments. *J. Phys. Condens. Matter* **32**, 413001 (2020).
30. A. I. Coldea, Electronic nematic states tuned by isoelectronic substitution in bulk $\text{FeSe}_{1-x}\text{S}_x$. *Front. Phys.* **8**, 528 (2021).
31. T. Hashimoto *et al.*, Bose-Einstein condensation superconductivity induced by disappearance of the nematic state. *Sci. Adv.* **6**, eabb9052 (2020).
32. T. M. McQueen *et al.*, Tetragonal-to-orthorhombic structural phase transition at 90 K in the superconductor $\text{Fe}_{1.01}\text{Se}$. *Phys. Rev. Lett.* **103**, 057002 (2009).
33. A. E. Böhmner *et al.*, Origin of the tetragonal-to-orthorhombic phase transition in FeSe: A combined thermodynamic and NMR study of nematicity. *Phys. Rev. Lett.* **114**, 027001 (2015).
34. S. Hosoi *et al.*, Nematic quantum critical point without magnetism in $\text{FeSe}_{1-x}\text{S}_x$ superconductors. *Proc. Natl. Acad. Sci. U.S.A.* **113**, 8139–8143 (2016).
35. M. A. Tanatar *et al.*, Origin of the resistivity anisotropy in the nematic phase of FeSe. *Phys. Rev. Lett.* **117**, 127001 (2016).
36. A. Baum *et al.*, Frustrated spin order and stripe fluctuations in FeSe. *Commun. Phys.* **2**, 14 (2019).
37. M. D. Watson *et al.*, Evidence for unidirectional nematic bond ordering in FeSe. *Phys. Rev. B* **94**, 201107 (2016).
38. A. I. Coldea, M. D. Watson, The key ingredients of the electronic structure of FeSe. *Annu. Rev. Condens. Matter Phys.* **9**, 125 (2018).
39. A. Fedorov *et al.*, Effect of nematic ordering on electronic structure of FeSe. *Sci. Rep.* **6**, 36834 (2016).
40. H. C. Xu *et al.*, Highly anisotropic and twofold symmetric superconducting gap in nematically ordered $\text{FeSe}_{0.93}\text{S}_{0.07}$. *Phys. Rev. Lett.* **117**, 157003 (2016).
41. P. O. Sprau *et al.*, Discovery of orbital-selective Cooper pairing in FeSe. *Science* **357**, 75–80 (2017).
42. W. Qing-Yan *et al.*, Interface-induced high-temperature superconductivity in single unit-cell FeSe films on SrTiO_3 . *Chin. Phys. Lett.* **29**, 037402 (2012).
43. J. F. Ge *et al.*, Superconductivity above 100 K in single-layer FeSe films on doped SrTiO_3 . *Nat. Mater.* **14**, 285–289 (2015).
44. D. H. Lee, Hunting down unconventional superconductors. *Science* **357**, 32–33 (2017).
45. A. Kostin *et al.*, Imaging orbital-selective quasiparticles in the Hund's metal state of FeSe. *Nat. Mater.* **17**, 869–874 (2018).
46. B. I. Halperin, C. M. Varma, Defects and the central peak near structural phase transitions. *Phys. Rev. B* **14**, 4030–4044 (1976).
47. R. J. Koch *et al.*, Room temperature local nematicity in FeSe superconductor. *Phys. Rev. B* **100**, 020501 (2019).
48. B. A. Frandsen, Q. Wang, S. Wu, J. Zhao, R. J. Birgeneau, Quantitative characterization of short-range orthorhombic fluctuations in FeSe through pair distribution function analysis. *Phys. Rev. B* **100**, 020504 (2019).
49. M. D. Watson *et al.*, Suppression of orbital ordering by chemical pressure in $\text{FeSe}_{1-x}\text{S}_x$. *Phys. Rev. B* **92**, 121108 (2015).
50. M. Yi *et al.*, Nematic energy scale and the missing electron pocket in FeSe. *Phys. Rev. X* **9**, 041049 (2019).
51. F. Kretzschmar *et al.*, Raman-scattering detection of nearly degenerate s -wave and d -wave pairing channels in iron-based $\text{Ba}_{0.6}\text{K}_{0.4}\text{Fe}_2\text{As}_2$ and $\text{Rb}_{0.8}\text{Fe}_{1.6}\text{Se}_2$ superconductors. *Phys. Rev. Lett.* **110**, 187002 (2013).
52. A. Hinojosa, J. Cai, A. V. Chubukov, Raman resonance in iron-based superconductors: The magnetic scenario. *Phys. Rev. B* **93**, 075106 (2016).
53. Y. Gallais, I. Paul, L. Chauvière, J. Schmalian, Nematic resonance in the Raman response of iron-based superconductors. *Phys. Rev. Lett.* **116**, 017001 (2016).
54. S. F. Wu *et al.*, Superconductivity and electronic fluctuations in $\text{Ba}_{1-x}\text{K}_x\text{Fe}_2\text{As}_2$ studied by Raman scattering. *Phys. Rev. B* **95**, 085125 (2017).
55. M. Ye *et al.*, Lattice dynamics of the $\text{Ta}_2\text{Ni}(\text{Se}_{1-x}\text{S}_x)_5$ excitonic insulator. arXiv:2102.07912 (16 February 2021).
56. V. Oganesyan, S. A. Kivelson, E. Fradkin, Quantum theory of a nematic Fermi liquid. *Phys. Rev. B* **64**, 195109 (2001).
57. D. L. Maslov, V. I. Yudson, A. V. Chubukov, Resistivity of a non-Galilean-invariant Fermi liquid near Pomeranchuk quantum criticality. *Phys. Rev. Lett.* **106**, 106403 (2011).
58. I. Paul, M. Garst, Lattice effects on nematic quantum criticality in metals. *Phys. Rev. Lett.* **118**, 227601 (2017).
59. X. Wang, E. Berg, Scattering mechanisms and electrical transport near an Ising nematic quantum critical point. *Phys. Rev. B* **99**, 235136 (2019).
60. W. L. Zhang *et al.*, On the origin of the electronic anisotropy in iron pnictide superconductors. arXiv:1410.6452 (23 October 2014).
61. F. Kretzschmar *et al.*, Critical spin fluctuations and the origin of nematic order in $\text{Ba}(\text{Fe}_{1-x}\text{Co}_x)_2\text{As}_2$. *Nat. Phys.* **12**, 560–563 (2016).
62. V. Cvetkovic, O. Vafek, Space group symmetry, spin-orbit coupling, and the low-energy effective Hamiltonian for iron-based superconductors. *Phys. Rev. B* **88**, 134510 (2013).
63. J. Hu, N. Hao, S_4 symmetric microscopic model for iron-based superconductors. *Phys. Rev. X* **2**, 021009 (2012).
64. W.-L. Zhang, W. R. Meier, T. Kong, P. C. Canfield, G. Blumberg, High- T_c superconductivity in $\text{CaKFe}_4\text{As}_4$ in absence of nematic fluctuations. *Phys. Rev. B* **98**, 140501 (2018).
65. C. C. Lee, W. G. Yin, W. Ku, Ferro-orbital order and strong magnetic anisotropy in the parent compounds of iron-pnictide superconductors. *Phys. Rev. Lett.* **103**, 267001 (2009).
66. W. Lv, J. Wu, P. Phillips, Orbital ordering induces structural phase transition and the resistivity anomaly in iron pnictides. *Phys. Rev. B* **80**, 224506 (2009).
67. T. Saito, S. Onari, H. Kontani, Orbital fluctuation theory in iron pnictides: Effects of As-Fe-As bond angle, isotope substitution, and Z^2 -orbital pocket on superconductivity. *Phys. Rev. B* **82**, 144510 (2010).
68. H. Yamase, R. Zeyher, Electronic Raman scattering from orbital nematic fluctuations. *Phys. Rev. B* **88**, 125120 (2013).
69. H. Kontani, Y. Yamakawa, Linear response theory for shear modulus C_{66} and Raman quadrupole susceptibility: Evidence for nematic orbital fluctuations in Fe-based superconductors. *Phys. Rev. Lett.* **113**, 047001 (2014).
70. A. Klein, S. Lederer, D. Chowdhury, E. Berg, A. Chubukov, Dynamical susceptibility of a near-critical nonconserved order parameter and quadrupole Raman response in Fe-based superconductors. *Phys. Rev. B* **98**, 041101 (2018).
71. Y. A. Pomeranchuk, On the stability of a Fermi liquid. *Sov. Phys. JETP* **8**, 361 (1958).
72. M. Udina, M. Grilli, L. Benfatto, A. V. Chubukov, Raman response in the nematic phase of FeSe. *Phys. Rev. Lett.* **124**, 197602 (2020).
73. R. Q. Xing, L. Classen, M. Khodas, A. V. Chubukov, Competing instabilities, orbital ordering, and splitting of band degeneracies from a parquet renormalization group analysis of a four-pocket model for iron-based superconductors: Application to FeSe. *Phys. Rev. B* **95**, 085108 (2017).